OPTICA

Spatiotemporal dissipation dynamics: a route to high-beam-quality and high-peak-power spatiotemporal mode-locked fiber lasers

GUOHAO FU,[1,2] YUHANG LI,[1,2] QIRONG XIAO,[1,2] DAN LI,[1,2] MALI GONG,[1,2] QIANG LIU,[1,2] STEFAN WABNITZ,[3] AND PING YAN[1,2,*]

[1]*Department of Precision Instrument, Tsinghua University, Beijing 100084, China*
[2]*State Key Laboratory of Precision Space-time Information Sensing Technology, Beijing 100084, China*
[3]*Department of Information Engineering, Electronics and Telecommunications, Università degli Studi di Roma Sapienza, 00184 Rome, Italy*
*pyan@mail.tsinghua.edu.cn

Spatiotemporal mode-locking (STML) opens a new avenue for implementing high-energy, high-peak-power mode-locked fiber oscillators. However, the compromised beam quality poses a critical limitation to their broader applications. This study presents a method for enhancing the beam quality of STML fiber lasers by employing spatiotemporal dissipation involving the quenching and reabsorption effects of multimode erbium-doped fibers. The proposed technique introduces spatiotemporal saturable absorption, achieving high beam quality without the stringent conditions required for Kerr beam self-cleaning (BSC). Integrating spatiotemporal dissipation with Kerr BSC, we demonstrate an all-anomalous-dispersion Er-doped STML fiber laser, which produces solitons with 6.7 nJ pulse energy (the intracavity solitons with 25.8 nJ pulse energy and >52.8 kW peak power), sub-500 fs pulse duration, and beam quality with $M_x^2/M_y^2 = 1.23/1.20$. To our knowledge, it is a record peak power for 1.5 µm band soliton lasers. Additionally, the approach enables the generation of noise-like pulses with $M_x^2/M_y^2 = 1.04/1.13$. This work not only advances our understanding of spatiotemporal dissipation dynamics in STML fiber lasers, but also paves the way toward high-performance STML fiber lasers, rendering them very attractive for applications.   © 2024 Optica Publishing Group under the terms of the

1. INTRODUCTION

Spatiotemporal mode-locked (STML) fiber lasers are drawing increasing interest within the field of mode-locked fiber lasers. With the expansion of spatial dimension, the cavity has richer $(3 + 1)$ dimensional nonlinear dynamics [1,2], including multidimensional laser attractors [3,4], multimode dissipative solitons [5–9], multiple-solitons [10], rogue waves [11], pulsating solitons [12], intracavity beam self-cleaning (BSC) [13–18], optical frequency combs [19], wavelength and pulse duration tunability [20–23], and pulse build-up processes [24]. In addition, STML can expand the degrees of freedom of laser mode-locking control [25], such as beam profile customization [26,27] and intracavity mode conversion [28] for applications ranging from imaging to detection, and many others [29].

In many of these applications, high-energy, high-peak-power ultrashort pulses are always attractive [30,31], since they can greatly alleviate the burdens on subsequent pulse amplifiers. Benefiting from the large effective core area and plenty of spatial mode channels of multimode fibers, STML fiber lasers are very promising for high-energy ultrashort pulse generation [32].

However, these multimode channels adversely lead to deteriorated beam quality for STML fiber lasers, which greatly hampers efficient coupling for the necessary amplification, and for many applications that require high beam quality. It has been recognized that BSC could play a significant role in STML fiber lasers with high beam quality. BSC exploits the Kerr nonlinearity in graded-index multimode fiber (GIMF), and it has been demonstrated in many experiments [14–18]. Furthermore, nonlinear pulse self-compression could boost high-peak-power intracavity pulse generation, thus promoting BSC in STML fiber lasers [16]. All of these mechanisms rely on the Kerr nonlinearity [33–35], a purely conservative process.

The occurrence of BSC in STML fiber lasers reported so far depends on reaching a condition of thermal equilibrium for the mode population in a conservative subsystem (the GIMF) of the cavity: as a result, BSC requires very high beam intensities and pulse peak powers [36]. On the other hand, stable $(3 + 1)$ dimensional solitons are formed from a balance between three-dimensional (3D) dispersion, nonlinearity, gain, and loss through the spatiotemporal dissipative dynamics of a multimode dissipative system [3,37,38]. Counting on the spatiotemporal dissipation of multimode dissipative systems, a delicate design of nonlinear 3D

gain and loss may provide a new route to achieve the BSC of STML fiber lasers. Some reports have verified that Kerr BSC may occur in both graded-index and step-index multimode gain fiber amplifiers with gain or loss [39–42].

1.5 µm band soliton mode-locked fiber lasers with all-anomalous dispersion have a natural ability to generate transform-limited pulses [32,43]. However, since the soliton energy is constrained by the soliton area theorem, ultrashort as well as high-energy solitons have been difficult to generate from single-mode mode-locked fiber lasers. Leveraging large-mode-area gain fiber has been considered a method for boosting soliton energy [44,45]. However, the output highest peak power of 1.5 µm region conventional soliton fiber lasers is still limited to 10 kW [44]. By using STML fiber lasers to alleviate the constraints of the soliton area theorem, higher output soliton energies and peak powers are expected to be generated.

In the present work, we will show that spatiotemporal dissipation could contribute to BSC together with the better-understood Kerr nonlinearity-induced BSC, giving rise to high-energy high-peak-power pulses with high beam quality. This spatiotemporal dissipation involves the quenching effect and reabsorption in highly doped multimode erbium-doped fibers, offering spatiotemporal intensity-dependent losses to modal pulses to gain high beam quality, which does not need the strict conditions that Kerr BSC requests, such as very high peak powers. Via the hybrid BSC (HBSC) mechanism, a STML fiber laser operating at 1.5 µm band is built, showing a high soliton energy of 6.7 nJ (the intracavity soliton energy and peak power are 25.8 nJ and >52.8 kW), pulse duration of <489 fs, and high beam quality of $M_x^2/M_y^2 = 1.23/1.20$. To the best of our knowledge, this represents a record peak power for 1.5 µm band soliton fiber lasers. Besides, high-peak-power noise-like pulses (NLPs) with beam quality $M_x^2/M_y^2 = 1.04/1.13$ in the STML fiber laser were also obtained, which further validates the BSC effect.

2. EXPERIMENTAL SETUP

The experimental setup of the Er-doped STML fiber laser is illustrated in Fig. 1. A 2 m long Er-doped fiber (EDF) (FORC, RAS, MM-EDF-20/125, NA = 0.142, core absorption = 12 dB/m at 976 nm) with a core diameter of 19 µm and a cladding diameter of 126 µm, supporting six linear polarization (LP) modes, was core-pumped with a 976 nm single-mode laser diode (LD) (maximum output power: 1.5 W). The EDF is a single-cladding step-index multimode fiber with a coiling diameter of 6 cm. The calculations reveal that the coiling losses for each mode are nearly negligible, and a loosely coiling case is also experimentally conducted, as detailed in Supplement 1 Section 2.1. The common and signal ports of the WDM are both 0.5 m step-index germanium doped fibers (GDF) (Nufern LMA-GDF-20/130-M, NA = 0.08), supporting three LP modes. Subsequently, an output coupler (OC) was adopted to extract 18% energy from the cavity for real-time spectral analysis by dispersive Fourier transform (DFT) and autocorrelation (AC) trace detection. Two collimators (CLs) are made from GIMF (OM4, 50/125, NA = 0.2, length = 0.5 m, 0.75 m). The GIMF length between EDF and OC is 3 m, and the GIMF length between OC and CL is 1.1 m. A half-wave plate (HWP), two quarter-wave plates (QWPs), and a polarization beam splitter (PBS) work as an artificial saturable absorber (SA) based on nonlinear polarization rotation (NPR). The free-space output from PBS was used for power, spectrum, and beam profile measurements.
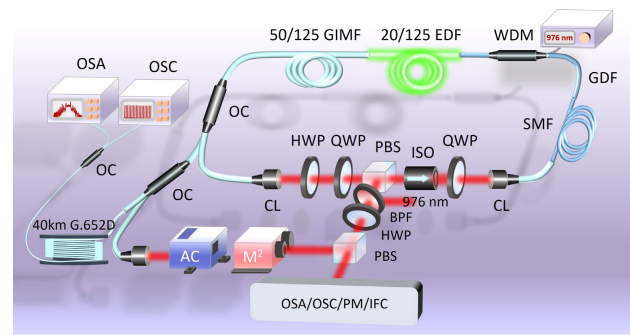

Fig. 1. Experimental setup of the Er-doped STML fiber laser. WDM: wavelength-division-multiplexer; EDF: erbium-doped fibers; GIMF: graded-index multimode fiber; OC: output coupler; CL: collimator; HWP: half-wave plate; QWP: quarter-wave plate; PBS: polarization beam splitter; ISO: isolator; SMF: single-mode fiber; GDF: germanium doped fibers; BPF: bandpass filter; OSA: optical spectrum analyzer; OSC: oscilloscope; PM: power meter; IFC: infrared camera.

Besides, an isolator guarantees counterclockwise propagation of the laser. After the second CL, a 6.6 m long single-mode fiber (SMF-28e) was carefully spliced, despite the large difference in the mode fields. Note that this SMF is necessary here, both to provide enough nonlinearity for NPR operation and to serve as a spatial filter for STML stabilization [46]. Despite the addition of the SMF, the fiber mismatch in the cavity leads to highly multimode excitation, resulting in an output laser with poor beam quality when the laser is operating in a linear regime. The total length of the cavity is 14.8 m, and all fibers have anomalous dispersion at 1.55 µm. For the measurement part, two ports, including the output port of the OC and the output port of the PBS, are used for characterizing pulses. For the DFT spectrum measurement, we used a 40 km long G.652D fiber with a DFT spectral resolution of 0.28 nm.

3. RESULTS

A. Spatiotemporal Saturable-Absorber Characteristics of Multimode EDF

In highly doped EDFs, erbium ions can easily cluster together to form ion pairs, leading to ion-pair-induced quenching (PIQ). The physical process of PIQ is that when an ion pair is excited onto the upper level [$^4I_{13/2}$ level, as shown in Fig. 3(a)], one ion will render energy to the other ion, so that the first ion drops down to the ground level ($^4I_{15/2}$), and the second one ion is excited onto a higher level ($^4I_{9/2}$), acting as the donor and the acceptor, respectively. Because of the short lifetime of $^4I_{9/2}$ level, the acceptor will quickly drop down onto a lower energy level (the upper level for lasing) via nonradiative transition. Therefore, PIQ causes a part of erbium ions to remain unpumped, so that the EDF behaves as a SA [47–52]. The mechanism involves saturable absorption by ground-level ions. At low signal intensities, this absorption is pronounced due to more ions on the ground level. However, with rising intensity, these ions are excited to the upper level, depleting the ground-state population; consequently, the absorption effect decreases and the transmission of the light through the active fiber increases. To numerically model this process, the EDF can be considered as a three-level laser system and a two-level absorber system, as shown in Fig. 2(a). This assumption is valid and equivalent to the role of PIQ. According to Ref. [47], the corresponding model can be written as follows:
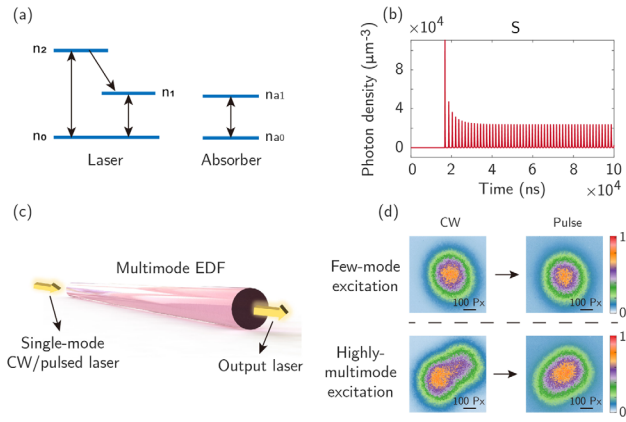
Fig. 2. Investigation of the beam self-cleaning effect induced by the saturable-absorber characteristic of multimode EDF. (a) The simplified energy levels of EDF. (b) Photon density evolution versus time when a laser is amplified in an EDF. (c) The schematic graph of BSC in a multimode EDF outside of the cavity. (d) Beam profiles of output CW and pulses from the EDF in the case of few-mode or highly multimode excitation, respectively.

$$\frac{dS}{dt} = \frac{\gamma}{\tau_{\mathrm{sp}}} n_1 + AS(n_1 - n_0) - \frac{S}{\tau_{\mathrm{loss}}} - A_a S(n_{a0} - n_{a1}), \quad (1)$$

$$\frac{dn_2}{dt} = \frac{1}{\tau_p} P(n_0 - n_1) - \frac{n_2}{\tau_{12}}, \quad (2)$$

$$\frac{dn_1}{dt} = \frac{n_2}{\tau_{12}} - \frac{n_1}{\tau_{\mathrm{sp}}} - AS(n_1 - n_0), \quad (3)$$

$$\frac{dn_{a1}}{dt} = -\frac{n_{a1}}{\tau_a} + A_a S(n_{a0} - n_{a1}), \quad (4)$$

$$N_0 = n_0 + n_1 + n_2, \quad (5)$$

$$N_{a0} = n_{a0} + n_{a1}, \quad (6)$$

where S is the photon density. n_0, n_1, n_2 are the population density on levels 0, 1, 2 of the laser system, and n_{a0} and n_{a1} are the population density on levels 0 and 1 of the absorber system. A and A_a are the stimulated emission factors of the laser and absorber, respectively. N_0, N_{a0} are the total population density of the laser state and absorber state, respectively. P is the pump factor. τ_a, τ_{loss}, τ_{sp}, τ_{12}, and τ_p are the decay time of level 1 of the absorber, photon decay time, spontaneous decay time of level 1, decay time of level 2 to level 1, and transit time for pumped ions, respectively. γ is the spontaneous emission capture ratio. The parameters that we used in our simulation are given in Supplement 1 Section 1.1.

Based on our model, the simulation result is shown in Fig. 2(b), which shows the variation of photon density with time when a laser is amplified in the EDF. As can be seen, a stable pulsation state is established after the system experiences an unstable period of about 20 µs. This pulsation state arising from PIQ means that EDF can work as a SA. The pulsation period can be tuned by the pump factor. The corresponding evolutions of ion population on each energy level are presented in Supplement 1 Section 1.1. From these results, one verifies that laser absorption is photon-density dependent, thus acting as a SA, eventually forming a pulse train. It is worth mentioning that PIQ-induced SA in EDF stems from

every position along the EDF, and therefore, the modulation depth and saturation intensity will increase with the EDF length [52].

In addition to PIQ, reabsorption can also make EDF behave as a SA. In contrast to PIQ, reabsorption occurs solely under conditions where the pump power is significantly lower than that of the signal light, and the active fiber length is relatively long: this leads to self-pulsation of the signal light, an effect that has been widely observed in fiber lasers [53,54]. This saturable absorption behavior due to the signal light reabsorption can be attributed to the non-uniform population inversion depending on the relative intensity of the pump and the signal [54]. In our setup, the 2 m long EDF is unidirectionally pumped with a calculated absorption of 24 dB at 976 nm, leading to a large power ratio of signal laser and residual pump (larger than 30 times measured experimentally). This is to say that the end of the gain fiber is weakly pumped but with high signal power, contributing to reabsorption-induced SA for the signal light. The model of reabsorption of EDF is given by Eq. (S1) in Supplement 1 Section 1.1.

Therefore, a mechanism of nonlinear dissipation is formed: the multimode EDF not only works as a gain medium offering energy, but it also works as a SA, which cuts a portion of the pulse energy. In a $(3+1)$ dimensional system, this dissipation is dependent on both space and time dimensions, namely, a spatiotemporal dissipation is achieved. In our simulation, to reduce complexity, we estimated the PIQ-induced and reabsorption-induced SA based on a uniform expression (which we call EDFSA). The spatiotemporal amplitude transmission of the SA can be represented as

$$T(x, y, z, T) = \sqrt{(1 - a_{\mathrm{ns}}) - \frac{M}{1 + \frac{P(x,y,z,T)}{P_{\mathrm{sat}}}}}. \quad (7)$$

Here x, y, z, and T are the space and time coordinates. a_{ns} is the non-saturable loss, M is the modulation depth, P_{sat} is the saturation power, and P is the laser power.

An experiment of investigation of the BSC effect induced by the spatiotemporal SA characteristic of EDF was conducted. The schematic is shown in Fig. 2(c). In the experiment, single-mode CW and femtosecond pulses with the same average power were separately injected into a 1 m long EDF (MM-EDF-20/125) without pumping. The initial modal excitation in the EDF can be tuned by altering the laser-coupling position on the input end face of the EDF. In the cases of few-mode or highly multimode excitation, the output beam profiles of the CW and pulses through EDF were measured, respectively, as shown in Fig. 2(d). As can be seen, in both cases the beam quality of output pulses is always improved when compared with that of a CW. A dynamic observation experiment was also conducted. The EDF was squeezed at its output end while the jitter of the output beam profile was observed. It is known that the fundamental mode is more robust to fiber squeezing than higher-order modes (HOMs) [16,34]. The experimental results show that during fiber squeezing, the beam profile in the pulsed state is more robust when compared with the CW state (Visualization 1, Visualization 2), which indicates that the fundamental-mode component in the pulsed state is higher and demonstrates the occurrence of BSC in the multimode EDF when pulses propagate in it.

B. Simulation of the STML Fiber Laser

Let us explain how the spatiotemporal dissipation arising from PIQ and reabsorption in EDF improves the beam quality of STML fiber

lasers. The principle is illustrated in Fig. 3(a). The BSC originates from a combination of EDFSA-BSC and Kerr-BSC. To simplify the simulation, we assume that amplification and saturable absorption come into play in two adjacent segments of the EDF (denoted as EDFA and EDFSA, respectively). Due to modal excitation caused by the fiber mismatching splice, six modal pulses are traveling in the EDF. In the EDFA segment, the intermodal walk-off gradually increases during amplification, and modal pulses separate in the spatiotemporal domain at the end of the amplifying segment. Subsequently, the pulses enter into the EDFSA. Because of the saturable absorption of the EDFSA, the transmission of the fundamental-mode pulse with a higher peak power in the EDFSA is higher than that of the HOMs pulse. Therefore, a beam quality improvement can be expected from these two cascaded EDF segments due to spatiotemporal dissipation. In the GIMF, Kerr BSC occurs owing to the nonlinear pulse self-compression, during which the intermodal interaction would transfer energy from the HOMs to the fundamental mode, and consequently it can improve the beam quality further [16,34].

To validate the above explanation and numerically show the BSC in EDFSA, we use two cases, i.e., a STML case and a continuous wave (CW) state. Only the first six LP modes in GIMF are considered to save the simulation time. Figure 3(b) shows the simulated intracavity pulse evolution for the STML case. After pulse amplification, the beam profile of the pulses at the end of the EDFA is shown in Fig. 3(c), exhibiting a beam quality M^2 of 1.36. Once the pulses pass after the EDFSA, EDFSA-induced BSC comes into play: the beam quality M^2 is improved to 1.15 [Fig. 3(d)], and then degraded slightly to 1.17 [Fig. 3(e)] owing to mode mismatch between the EDF and the GIMF. However, the situation is different for the CW case. This case is achieved by
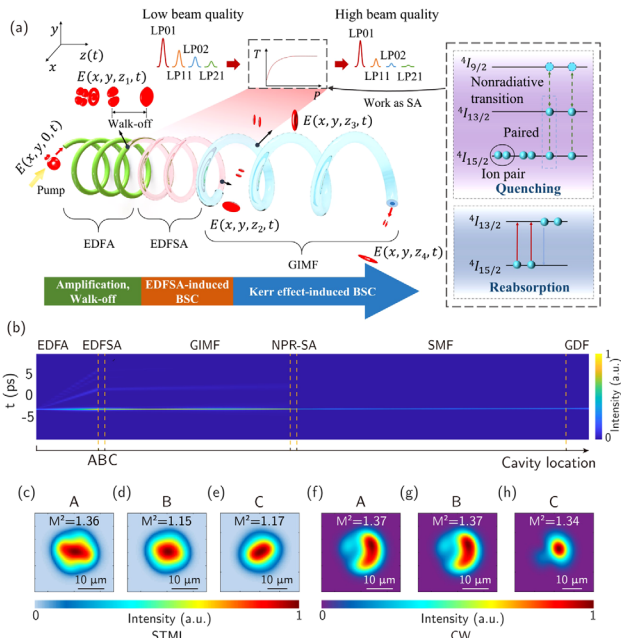
setting the modulation depth of NPR-SA to zero and injecting an initial direct current amplitude. The simulated beam profiles at the end of the EDFA, after the EDFSA, and at the beginning of the GIMF are shown in Figs. 3(f)–3(h), respectively. These results show that in the CW case the EDFSA cannot enhance the beam quality in the cavity. This is because in the CW case, all modal pulse intensities are too low to saturate the EDFSA; hence, losses for all modal pulses are high and nearly the same, and thus the beam quality remains nearly unchanged.

Then soliton dynamics involved are studied. One should mention that the solitons are not multimode solitons, as multimode solitons do not change pulse shape and do not spread apart in a GIMF [55]. The spectral evolution of the solitons in the cavity is shown in Fig. 4(a). As can be seen, the solitons present obvious spectral breathing because of the competition between dispersion-induced negative chirp and nonlinearity-induced positive chirp in the high-energy case [56]. Figure 4(b) displays output mode-resolved soliton spectra from the end of GIMF, where the spectrum of LP01 mode presents a symmetric multi-peak feature. The spectral peaks stem from Kelly sidebands of the LP01 mode soliton, as discussed in Supplement 1 Section 1.3. Because of the large intermodal dispersion in the EDF, the modal pulses disperse quickly, as shown in Fig. 4(c). Subsequently, the modal excitation between the EDF and GIMF alters the walk-off condition. The excited pulses then travel in the GIMF with small intermodal dispersion, so they disperse slowly. However, after they enter into the SMF, intermodal walk-off is completely compensated for via the large spatial filter stemming from the fusion between the GIMF and the SMF. Figure 4(d) shows the dramatic evolution of the pulse duration and the spectral bandwidth in the cavity. Thanks to nonlinear pulse amplification in the EDF and the opposite signs of the nonlinearity-induced chirp and of dispersion-induced chirp, nonlinear pulse self-compression occurs in the EDF and the GIMF. In Fig. 4(e), we can see the modal pulses in the time domain before [the left half of Fig. 4(e)] and after [the right half of Fig. 4(e)] the EDFSA. The result indicates that due to the EDFSA, the loss of the
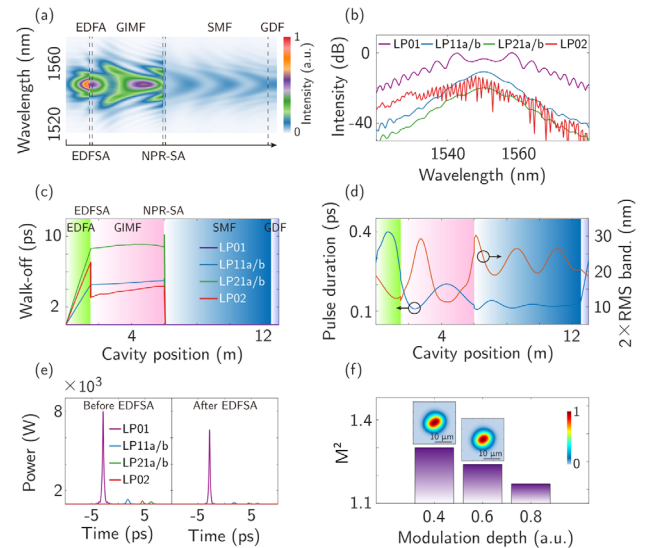

Fig. 3. Simulation of beam self-cleaning in the STML fiber laser. (a) The principle graph of hybrid beam self-cleaning in the STML fiber laser. In EDFSA, the higher the peak power P, the higher transmission T a modal pulse has. In GIMF, the Kerr beam self-cleaning occurs. (b) Modal pulses evolution in the cavity, when mode-locking is realized. (c)–(e) Beam profiles of mode-locking pulses at positions A, B, and C of the cavity, respectively. Position A: at the end of EDF; position B: after EDFSA; position C: at the beginning of GIMF. (f)–(h) Beam profiles of the continuous wave at positions A, B, and C of the cavity, respectively.

Fig. 4. Simulation of the characteristics of STML solitons. (a) Spectral evolution of the soliton in the cavity. (b) Output mode-resolved spectra. (c) Evolution of walk-off among modal pulses in the cavity. (d) Evolution of the pulse duration and spectral bandwidth in the cavity. (e) The left and right half figures show the modal pulses before and after EDFSA, respectively. (f) Beam quality of modal pulses at the beginning of the GIMF versus modulation depth of the EDFSA.

HOM pulses is higher than the fundamental-mode pulse, which leads to BSC. A longer EDF has a higher modulation depth for the EDFSA. The effect of modulation depth on the BSC effect is investigated [Fig. 4(f)]. Notably, the BSC effect is enhanced whenever the modulation depth is larger, indicating a relatively long EDF is more favorable for the observation of BSC.

C. Experimental Results

After the experimental setup is built, by increasing the pump power to 400 mW and adjusting the wave plates, a stable mode-locking state is obtained. The single-pulse state can be maintained until the pump power reaches 900 mW. When the pump power reaches 900 mW, the highest single-pulse energy is 6.7 nJ, with an average power of 93 mW [Fig. 5(g)]. The pulse spectra and pulse trains sampled at three spots on the beam profile are shown in Figs. 5(a) and 5(b), respectively. Spot 1 is on the center of the beam profile, while the other two spots (S2, S3) are on either side of the center. The distinct spectral component and synchronous pulse train at these spots validate the achievement of STML. The clearly discernible presence of Gordon-Kelly sidebands verifies the occurrence of soliton STML [57,58]. Once the pump power and wave plates are fixed, the pulse train is very stable, presenting a repetition rate of 13.97 MHz, which corresponds to the cavity length of 14.8 m, and a high signal-to-noise ratio of 51 dB in its radio-frequency spectrum [Fig. 5(c)]. The AC trace shows a pulse duration of 489 fs [Fig. 5(d)]. The signal power out from the intracavity OC is 65 mW, so that the intracavity signal power is 361 mW according to the output ratio of the OC. Hence, the intracavity energy can be calculated to be as high as 25.8 nJ, with a peak power of 52.8 kW. Considering the pulse broadening in the output fiber of the OC, the peak power is even higher than 52.8 kW. Such high peak power favors the occurrence of HBSC effects. As observed, some small dispersed satellite pulses appear in the AC trace. These satellite pulses are HOMs pulses, which still remain after the function of BSC. And because of modal dispersion, they are dispersed in the time domain. The M^2 measurement result of the output solitons is displayed in Fig. 5(e), showing a good beam quality with $M_x^2 = 1.23$ and $M_y^2 = 1.20$. The inset in Fig. 5(e) is the beam profile of the STML pulses, which shows a perfect Gaussian-shape intensity distribution (also can be seen in Visualization 3). However, if we adjust the wave plates to destroy the STML state and then obtain a CW state, the beam quality deteriorates quickly [Fig. 5(f)]. The corresponding beam quality is poor, with $M_x^2 = 2.12$ and $M_y^2 = 1.90$. In this case the beam profile exhibits a speckled intensity distribution, which confirms the poor beam quality. As the coiling of the EDF is released to 12 cm, the beam quality of STML pulses still remains as good as in this case (Supplement 1 Section 2.1), while the beam quality of CW still remains poor. This indicates that the BSC effect observed in our experiment cannot be attributed to the coiling of EDF, but to spatiotemporal dissipative BSC and Kerr-induced BSC. Besides, the poor beam quality of the CW suggests that inserting a SMF in the cavity does not mean that a high-beam-quality laser output is obtained, due to the highly multimode excitation between different intracavity fibers. The experimental results are in good agreement with our simulations. Because of the requirement of high laser intensity, BSC only occurs in the STML state but not in
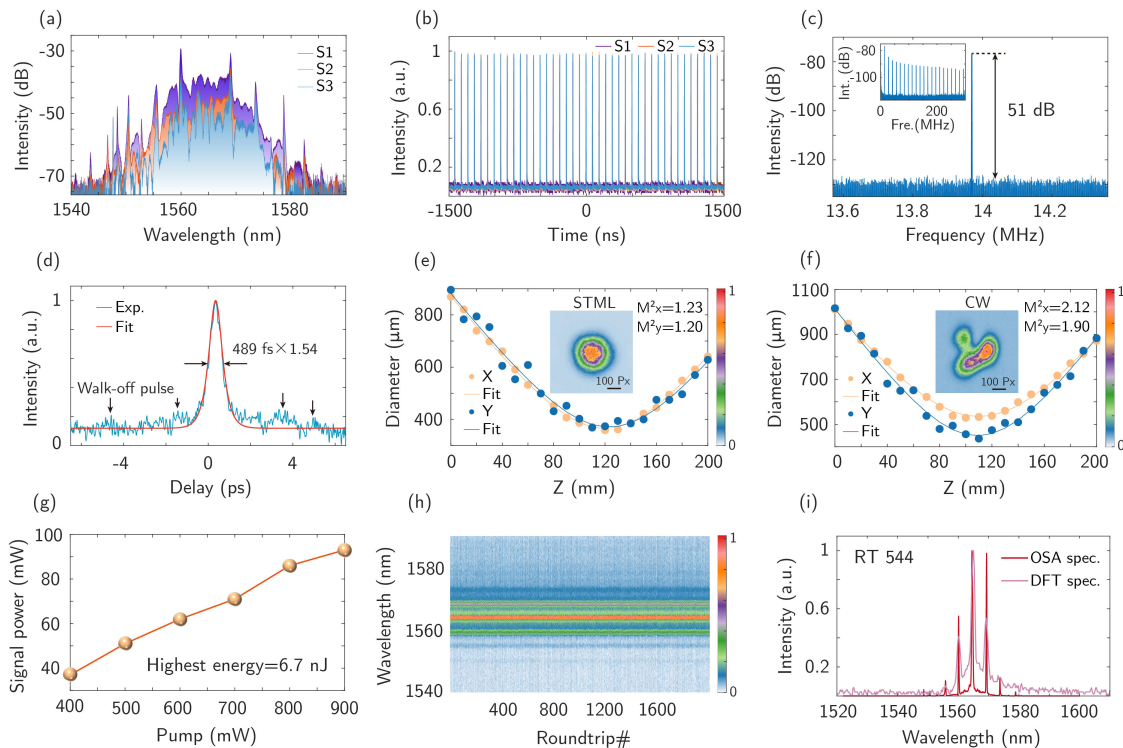

Fig. 5. Characteristics of STML solitons. (a) STML spectra are sampled at three different spots on the beam profile. Spot 1 (S1) is on the center of the beam profile, while the other two spots (S2, S3) are on either side of the center. (b) The corresponding pulse trains for these spots. (c) Radio-frequency spectrum of the STML pulses. The inset is a radio-frequency spectrum with a large span. (d) Autocorrelation trace of the soliton pulse with sech² fitting. (e) M^2 measurement result of STML pulses. The inset is the corresponding beam profile. (f) Beam profile of a CW state. The inset is the corresponding beam profile. (g) Output signal power versus pump power. (h) Shot-to-shot DFT spectral evolution of the STML soliton. (i) A single-shot DFT spectrum at roundtrip 544 and the corresponding spectrum measured by OSA.

the CW state. In addition, shot-to-shot spectra by using the DFT technique are measured [Fig. 5(h)]. The single-shot spectrum at roundtrip 544 is depicted in Fig. 5(i), where the measured OSA spectrum is also shown. Note that the DFT spectrum matches the OSA spectrum very well. The spectra are different from that out of the PBS port because of the spatial filter between the GMIF and the G.652D fiber.

As we delicately adjust the wave plates, the STML pulse starts to split and a multiple-pulse state is generated [Fig. 6(a)]. The M^2 measurement result shows that its beam quality M_x^2/M_y^2 is 1.25/1.21 [Fig. 6(b)]. The corresponding beam profile exhibits a condensed intensity distribution, but the beam quality is a little lower when compared to the single-pulse state. This is because multiple pulses have a comparatively lower peak power; thus the effect of HBSC is reduced. If the wave plates are continuously rotated to a state, chaotic pulses are obtained [Fig. 6(c)]. This chaotic state is characterized by random high peak pulses, which strengthens the HBSC effect. Its M^2 measurement result manifests a better beam quality with $M_x^2/M_y^2 = 1.07/1.05$ [Fig. 6(d)].

The influence of the EDF length on the EDFSA-induced BSC is experimentally demonstrated. Two other lengths of EDF were investigated in the STML fiber laser: a 1.5 m, and a 1 m EDF. By regulating the pump power and the angles of wave plates, STML is achieved for both cases. Figures 6(e)–6(g) are the STML pulse spectrum, pulse train, and M^2 measurement result for the STML fiber laser with a 1.5 m EDF, respectively, while Figs. 6(h)–6(j) show the results for the laser with a 1 m EDF. The output pulse energy of the two STML lasers is nearly the same as that of the STML fiber laser with a 2 m EDF. The pulse trains present that the generation of stable single-pulse STML states is achieved. In the 1.5 m EDF case, the beam quality M_x^2/M_y^2 of the STML pulses is 1.34/1.20, while in the 1 m EDF case, the M_x^2/M_y^2 is 1.42/1.42. Also, as can be seen, with decreasing the EDF length, the beam profile of STML pulses deviates from a Gaussian beam [Figs. 6(g) and 6(j)]. The beam quality results show the same tendency as in our simulations:

using longer EDFs improves the BSC effect, which in turn brings a better beam quality. This can be clearly seen in Fig. 6(k), where the M^2 for the three STML fiber lasers with different EDF lengths are compared.

The characteristics of the STML fiber laser with a long cavity were also investigated. The total cavity length was increased up to 35.7 m by using a longer SMF. After the experimental setup was established, by tuning the angles of the wave plates and the pump power, nanosecond pulses were obtained (more details are shown in Supplement 1 Section 2.2). Then, by manipulating the wave plates further, NLPs were also generated. In recent years, NLPs have been studied in STML fiber lasers: they exhibit a broad spectrum and high output powers [17,18,59]. It was demonstrated that NLPs consist of many high-peak-power random-distributed ultrashort pulses [60,61]. When the pump power is 1.5 W, the highest output power of the NLPs is 316 mW, corresponding to the highest energy of 54.5 nJ. The spectrum and pulse train of the NLPs are depicted in Figs. 7(a) and 7(b). The AC trace of a NLP is well-known, consisting of a narrow spike and a broad pedestal (see Supplement 1 Section 2.2). The beam quality factor M_x^2/M_y^2 of the NLPs is 1.04/1.13 [Fig. 7(c)], which is better than STML solitons. Noise-like mode-locking is prone to generate high-peak-power pulses; in turn, these pulses are more often likely to induce nonlinear beam cleaning inside the cavity [11]. If we adjust the wave plates to get CW states, the beam quality quickly deteriorates, with a poor beam quality of $M_x^2/M_y^2 = 1.62/1.88$ [Fig. 7(d)].

4. DISCUSSION AND CONCLUSION

Spatiotemporal dissipative BSC may occur in other rare-earth-doped STML fiber lasers, such as thulium-doped fibers, which are capable of operating as gain-fiber-based saturable absorbers (GFSAs), owing to their quenching and reabsorption characteristics. For other quenching-free rare-earth-doped fibers such as ytterbium-doped fiber, the reabsorption-induced SA effect may be
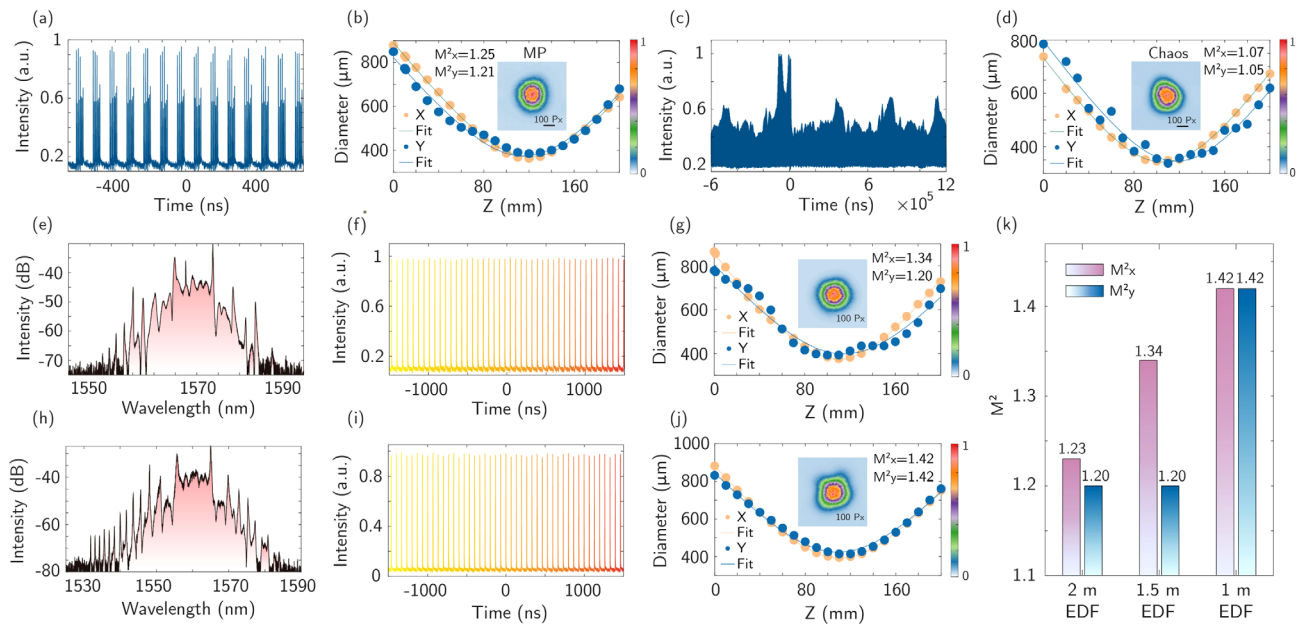

Fig. 6. Beam quality of multiple pulses and chaotic pulses, and the influence of EDF length on the beam quality of STML solitons. (a) Multiple-pulses pulse train. (b) M^2 measurement result of the multiple pulses. (c) Chaotic pulse train and (d) the corresponding M^2 measurement result. (e)–(g) STML spectrum, pulse train, and M^2 measurement result, respectively, for the STML fiber laser with a 1.5 m EDF. (h)–(j) Results for a 1 m EDF. (k) M^2 versus EDF length.
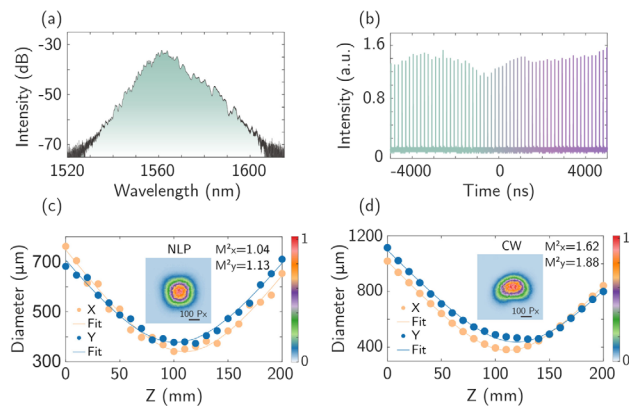
Fig. 7. Characteristics of NLPs. (a) NLP spectrum. (b) The corresponding pulse train. (c), (d) M^2 measurement results of NLPs and CW, respectively.

facilitated for BSC. The spatiotemporal dissipative BSC effect of the GFSA is conditional. The prerequisite for the spatiotemporal dissipative BSC is that the gain fiber should be multimode. A relatively long length of gain fiber needs to be used, in order to improve the modulation depth and saturation intensity of the GFSA, and leave a segment of weakly pumped gain fiber in order to produce reabsorption. Moreover, achieving a superior beam quality in STML fiber lasers hinges on optimal initial modal excitations. Previous studies have demonstrated that a fundamental-mode-dominated initial excitation enhances the Kerr BSC effect [36,62], a principle that extends to the spatiotemporal dissipative BSC as well. Especially for the spatiotemporal dissipative BSC, the intensity of the fundamental mode in the gain fiber needs to be the highest; otherwise, the beam quality may deteriorate. A beam with a better beam quality will get more improvement in beam quality after the GFSA, as discussed in Supplement 1 Section 1.2. Consequently, the cavity architecture must be meticulously engineered to prevent speckled excitation due to a high NA mismatch between different fibers or poor spatial coupling, as this could result in a weak or ineffective BSC. Last but not least, although BSC is improved by increasing the fiber length, the fiber should not be too long, in order to avoid excessive loss.

In summary, a spatiotemporal dissipation method utilizing the quenching and reabsorption effects of multimode erbium-doped fiber is proposed for enhancing the beam quality of STML fiber lasers. The spatiotemporal dissipation acts as an equivalent SA, offering spatiotemporal intensity-dependent losses to modal pulses, which leads to improved beam quality. This mode-selective SA mechanism does not need the strict conditions that Kerr beam self-cleaning (BSC) requests. In concert with the Kerr BSC, our HBSC method was used to demonstrate near-single-mode high-energy high-peak-power STML emission from an all-anomalous-dispersion fiber laser. Soliton pulses, nanosecond pulses, and NLPs were obtained in the cavity, exhibiting different properties. Assisted by the spatiotemporal dissipation, higher pulse energies, higher beam qualities, and other interesting properties can be expected for normal-dispersion and mid-infrared STML fiber lasers. Our STML fiber laser architecture will advance our understanding of spatiotemporal dissipation dynamics in STML fiber lasers, and pave the way toward high-performance STML fiber lasers, rendering them very attractive for applications.

Disclosures. The authors have no conflicts to disclose.

Data availability. The data that support the findings of this study are available on request from the corresponding author. The data are not publicly available.

Supplemental document. See Supplement 1 for supporting content.

REFERENCES

1. Y. Shen, Q. Zhan, L. G. Wright, *et al.*, "Roadmap on spatiotemporal light fields," J. Opt. **25**, 093001 (2023).
2. B. Fu, C. Shang, H. Liu, *et al.*, 'Recent advances and future outlook in mode-locked lasers with multimode fibers," Appl. Phys. Rev. **10**, 041305 (2023).
3. L. G. Wright, P. Sidorenko, H. Pourbeyram, *et al.*, "Mechanisms of spatiotemporal mode-locking," Nat. Phys. **16**, 565–570 (2020).
4. K. Krupa, A. Tonello, A. Barthélémy, *et al.*, "Multimode nonlinear fiber optics, a spatiotemporal avenue," APL Photonics **4**, 110901 (2019).
5. L. G. Wright, D. N. Christodoulides, and F. W. Wise, "Spatiotemporal mode-locking in multimode fiber lasers," Science **358**, 94–97 (2017).
6. U. Teğin, E. Kakkava, B. Rahmani, *et al.*, "Spatiotemporal self-similar fiber laser," Optica **6**, 1412–1415 (2019).
7. C. Gao, B. Cao, Y. Ding, *et al.*, "All-step-index-fiber spatiotemporally mode-locked laser," Optica **10**, 356–363 (2023).
8. H. Zhang, Y. Zhang, J. Peng, *et al.*, "All-fiber spatiotemporal mode-locking lasers with large modal dispersion," Photon. Res. **10**, 483–490 (2022).
9. B. Ge, Y. Lou, S. Guo, *et al.*, "A high-energy, wide-spectrum, spatiotemporal mode-locked fiber laser," Micromachines **15**, 644 (2024).
10. Y. Ding, X. Xiao, P. Wang, *et al.*, "Multiple-soliton in spatiotemporal mode-locked multimode fiber lasers," Opt. Express **27**, 11435–11446 (2019).
11. U. Teğin, P. Wang, and L. V. Wang, "Real-time observation of optical rogue waves in spatiotemporally mode-locked fiber lasers," Commun. Phys. **6**, 60 (2023).
12. W.-Y. He, G. X. Liu, J. W. Wu, *et al.*, "Spatiotemporal dual-periodic soliton pulsation in a multimode fiber laser," Opt. Lett. **49**, 1575–1578 (2024).
13. R. Guenard, K. Krupa, R. Dupiol, *et al.*, "Nonlinear beam self-cleaning in a coupled cavity composite laser based on multimode fiber," Opt. Express **25**, 22219–22227 (2017).
14. U. Teğin, B. Rahmani, E. Kakkava, *et al.*, "Single-mode output by controlling the spatiotemporal nonlinearities in mode-locked femtosecond multimode fiber lasers," Adv. Photonics **2**, 056005 (2020).
15. M. Qiu, M. Chen, and Z. Zhang, "Wavelength-dependent Kerr beam self-cleaning in spatiotemporal mode-locked multimode fiber laser," IEEE Photonics Technol. Lett. **33**, 1073–1076 (2021).
16. G. Fu, T. Qi, W. Yu, *et al.*, "Beam self-cleaning of 1.5 μm high peak-power spatiotemporal mode-locked lasers enabled by nonlinear compression and disorder," Laser Photonics Rev. **17**, 2200987 (2023).
17. H. Zhang, J. Lu, J. Peng, *et al.*, "Investigation of high-power spatiotemporal mode-locking with high beam quality," Laser Photonics Rev. **17**, 2300017 (2023).
18. Y. Fan, P. Zhang, Y. Liu, *et al.*, "Noise-like pulses generation and its beam self-cleaning effect in an all-fiber multimode cavity with a figure-8 scheme," Opt. Laser Technol. **169**, 110017 (2024).
19. J. Sun, G. Wang, J. Chao, *et al.*, "Buildup of multiple spatiotemporal nonlinear dynamics in an all-fiber multimode laser," Opt. Lett. **48**, 6019–6022 (2023).
20. Q. Zeng, Z. Tang, D. Ouyang, *et al.*, "Wavelength-tunable spatiotemporal mode-locking in a large-mode-area Er: ZBLAN fiber laser at 2.8 μm," Opt. Lett. **49**, 1117–1120 (2024).
21. L. Yu, Z. Tang, Q. Zeng, *et al.*, "Spatiotemporal mode-locking in a linear-cavity Er: ZBLAN fiber laser," J. Lightwave Technol. **42**, 4966–4971 (2024).
22. Z.-L. Ma, J. G. Long, W. Lin, *et al.*, "Tunable spatiotemporal mode-locked fiber laser at 1.55 μm," Opt. Express **29**, 9465–9473 (2021).
23. X. Zhang, Z. Wang, C. Shen, *et al.*, "Spatiotemporal self-mode-locked operation in a compact partial multimode Er-doped fiber laser," Opt. Lett. **47**, 2081–2084 (2022).

24. K. Liu, X. Xiao, Y. Ding, *et al.*, "Buildup dynamics of multiple solitons in spatiotemporal mode-locked fiber lasers," Photon. Res. **9**, 1898–1906 (2021).

25. L. G. Wright, W. H. Renninger, D. N. Christodoulides, *et al.*, "Nonlinear multimode photonics: nonlinear optics with many degrees of freedom," Optica **9**, 824–841 (2022).

26. X. Wei, J. C. Jing, Y. Shen, *et al.*, "Harnessing a multi-dimensional fibre laser using genetic wavefront shaping," Light Sci. Appl. **9**, 149 (2020).

27. Y. Lou, B. Ge, S. Gou, *et al.*, "Ultrafast flat-top beam emission with an all-fiber multimode laser," ACS Photonics **11**, 1901–1908 (2024).

28. D. Xing, M. Feng, C. Liu, *et al.*, "Spatiotemporal mode-locked fiber laser based on dual-resonance coupling long-period fiber grating," Opt. Express **31**, 7134–7143 (2023).

29. J. C. Jing, X. Wei, and L. V. Wang, "Spatio-temporal-spectral imaging of non-repeatable dissipative soliton dynamics," Nat. Commun. **11**, 2059 (2020).

30. Z. Li, Y. Leng, and R. Li, "Further development of the short-pulse petawatt laser: trends, technologies, and bottlenecks," Laser Photonics Rev. **17**, 2100705 (2023).

31. W. Fu, L. G. Wright, P. Sidorenko, *et al.*, "Several new directions for ultrafast fiber lasers," Opt. Express **26**, 9432–9463 (2018).

32. A. Blanco-Redondo, C. M. Sterkede, C. Xu, *et al.*, "The bright prospects of optical solitons after 50 years," Nat. Photonics **17**, 937–942 (2023).

33. M. Zitelli, F. Mangini, and S. Wabnitz, "Statistics of modal condensation in nonlinear multimode fibers," Nat. Commun. **15**, 1149 (2024).

34. K. Krupa, A. Tonello, B. M. Shalaby, *et al.*, "Spatial beam self-cleaning in multimode fibres," Nat. Photonics **11**, 237–241 (2017).

35. H. Pourbeyram, P. Sidorenko, F. O. Wu, *et al.*, "Direct observations of thermalization to a Rayleigh–Jeans distribution in multimode optical fibres," Nat. Phys. **18**, 685–690 (2022).

36. A. Fusaro, J. Garnier, K. Krupa, *et al.*, "Dramatic acceleration of wave condensation mediated by disorder in multimode fibers," Phys. Rev. Lett. **122**, 123902 (2019).

37. V. L. Kalashnikov and S. Wabnitz, "Distributed Kerr-lens mode locking based on spatiotemporal dissipative solitons in multimode fiber lasers," Phys. Rev. A **102**, 023508 (2020).

38. V. L. Kalashnikov and S. Wabnitz, "Stabilization of spatiotemporal dissipative solitons in multimode fiber lasers by external phase modulation," Laser Phys. Lett. **19**, 105101 (2022).

39. R. Guenard, K. Krupa, R. Dupiol, *et al.*, "Kerr self-cleaning of pulsed beam in an ytterbium doped multimode fiber," Opt. Express **25**, 4783–4792 (2017).

40. H. Haig, N. Bender, Y. H. Chen, *et al.*, "Gain-induced Kerr beam cleaning in a femtosecond fiber amplifier," J. Opt. Soc. Am. B **40**, 1510–1517 (2023).

41. A. Niang, T. Mansuryan, K. Krupa, *et al.*, "Spatial beam self-cleaning and supercontinuum generation with Yb-doped multimode graded-index fiber taper based on accelerating self-imaging and dissipative landscape," Opt. Express **27**, 24018–24028 (2019).

42. A. Niang, D. Modotto, A. Tonello, *et al.*, "Spatial beam self-cleaning in tapered Yb-doped GRIN multimode fiber with decelerating nonlinearity," IEEE Photon. J. **12**, 1–8 (2020).

43. A. Grudinin and S. Gray, "Passive harmonic mode locking in soliton fiber lasers," J. Opt. Soc. Am. B **14**, 144–154 (1997).

44. M. Fermann, A. Galvanauskas, and M. Hofer, "Ultrafast pulse sources based on multi-mode optical fibers," Appl. Phys. B **70**, S13–S23 (2000).

45. B. Ortaç, J. Limpert, S. Jetschke, *et al.*, "High-energy soliton pulse generation with a passively mode-locked Er/Yb-doped multifilament-core fiber laser," Appl. Phys. B **98**, 27–31 (2010).

46. Y. Wu, D. N. Christodoulides, and F. W. Wise, "Multimode nonlinear dynamics in spatiotemporal mode-locked anomalous-dispersion lasers," Opt. Lett. **47**, 4439–4442 (2022).

47. D. Marcuse, "Pulsing behavior of a three-level laser with saturable absorber," IEEE J. Quantum Electron. **29**, 2390–2396 (1993).

48. G. Fu, G. Li, W. Yu, *et al.*, "301 W narrow-linewidth in-band pumped Er: Yb co-doped fiber amplifier at 1585 nm and related modeling for dynamics study and optimization," High Power Laser Sci. Eng. **12**, e40 (2024).

49. S. Colin, E. Contesse, P. Le Boudec, *et al.*, "Evidence of a saturable-absorption effect in heavily erbium-doped fibers," Opt. Lett. **21**, 1987–1989 (1996).

50. M. Durán-Sánchez, B. Posada-Ramírez, R. I. Álvarez-Tamayo, *et al.*, "Soliton molecules in self-mode-locked ring-cavity Er/Yb double-clad fiber laser," IEEE Photon. J. **11**, 1504608 (2019).

51. J. Shang, T. Feng, S. Zhao, *et al.*, "An investigation into self-pulsing behavior in an Er-doped ring laser," Appl. Phys. Express **13**, 112006 (2020).

52. D. C. Kirsch, A. Bednyakova, P. Varak, *et al.*, "Gain-controlled broadband tuneability in self-mode-locked Thulium-doped fibre laser," Commun. Phys. **5**, 219 (2022).

53. S. Jackson, "Direct evidence for laser reabsorption as initial cause for self-pulsing in three-level fibre lasers," Electron. Lett. **38**, 1–2 (2002).

54. F. Brunet, Y. Taillon, P. Galarneau, *et al.*, "A simple model describing both self-mode locking and sustained self-pulsing in ytterbium-doped ring fiber lasers," J. Lightwave Technol. **23**, 2131–2138 (2005).

55. W. H. Renninger and F. W. Wise, "Optical solitons in graded-index multimode fibres," Nat. Commun. **4**, 1719 (2013).

56. G. P. Agrawal, "Nonlinear fiber optics," in *Nonlinear Science at the Dawn of the 21st Century* (Springer, 2000), pp. 195–211.

57. J. P. Gordon, "Dispersive perturbations of solitons of the nonlinear Schrödinger equation," J. Opt. Soc. Am. B **9**, 91–97 (1992).

58. S. Kelly, "Characteristic sideband instability of the periodically amplified (average) soliton," in *International Quantum Electronics Conference* (Optica Publishing Group, 1992), paper TuH3.

59. Y. Liu, L. Jin, Y. Sui, *et al.*, "All-fiber spatiotemporal mode-locked based on mamyshev mechanism with high energy noise-like pulse generation at 1550 nm," Opt. Commun. **552**, 130074 (2024).

60. M. Horowitz, Y. Barad, and Y. Silberberg, "Noiselike pulses with a broadband spectrum generated from an erbium-doped fiber laser," Opt. Lett. **22**, 799–801 (1997).

61. Y. Jeong, L. A. Vazquez-Zuniga, S. Lee, *et al.*, "On the formation of noise-like pulses in fiber ring cavity configurations," Opt. Fiber Technol. **20**, 575–592 (2014).

62. Y. Leventoux, A. Parriaux, O. Sidelnikov, *et al.*, "Highly efficient few-mode spatial beam self-cleaning at 1.5 μm," Opt. Express **28**, 14333–14344 (2020).